



Effect of various leg geometries on thermo-mechanical and power generation performance of thermoelectric devices



Ugur Erturun ^{a,*}, Kaan Erermis ^b, Karla Mossi ^a

^a Department of Mechanical and Nuclear Engineering, Virginia Commonwealth University, Richmond, VA, USA

^b Department of Mechanical Engineering, Virginia Military Institute, Lexington, VA, USA

HIGHLIGHTS

- Thermoelectric modules with various leg geometries were modeled and analyzed for two different temperature gradients.
- Disparities in temperature distributions, power outputs, and conversion efficiencies were limited.
- Magnitudes and distributions of thermal stresses in the legs were significantly affected by changing leg geometries.
- Thermal stress levels were smaller in the cylindrical and trapezoidal prism legs compare to the rectangular prism legs.

ARTICLE INFO

Article history:

Received 1 March 2014

Accepted 9 July 2014

Available online 17 July 2014

Keywords:

Thermoelectric devices

Peltier modules

thermal stress

thermoelectric power generation

finite-element analysis

ABSTRACT

This study aims to investigate possible effect of various thermoelectric leg geometries on thermo-mechanical and power generation performances of thermoelectric devices. For this purpose, thermoelectric modules with various leg geometries were modeled and finite-element analyses for two different temperature gradients were carried out using ANSYS. Temperature distributions, power outputs, conversion efficiencies, thermal stresses in the legs were evaluated for each model. Significant differences in magnitudes and distributions of the thermal stresses in the legs occurred due to changing leg geometries. Thermal stresses in the rectangular prism and the cylindrical legs were 49.9 MPa and 43.3 MPa respectively for the temperature gradient of 100 °C.

© 2014 Elsevier Ltd. All rights reserved.

1. Introduction

Environmental challenges, such as global warming, growing demand on energy, and diminishing oil sources have accelerated research on alternative energy conversion methods. Meanwhile, significant amount of energy is wasted during energy conversion processes due to technological limitations. Particularly in vehicles, more than 50% of the fuel energy [1] dissipates to the environment through exhaust and cooling systems as heat. Recovering some amount of wasted heat and converting it into useful energy such as electricity could increase overall efficiency of energy conversion systems and reduce demand on fossil fuels and natural resources. Thermoelectric power generation is an appropriate and promising method to convert wasted heat into electrical energy. Imposed temperature gradient through a thermoelectric device (module) produces electrical potential through the Seebeck effect, discovered

by Thomas J. Seebeck. Thermoelectric devices can also be used for cooling/heating purposes utilizing Peltier effect.

Based on the application, thermoelectric devices can be used for cooling, heating, power generation, and sensing [2]. The benefits include being solid state (no moving parts), silent, maintenance free and light weight. These characteristics attract attention to thermoelectric devices from industries including defense, aerospace, electronics, and automotive. Temperature controlled car seats, electronic device cooling, thermal management, waste heat recovery from hot chimneys, thermoelectric cogeneration systems and energy harvesting from human body heat are some of the existing and potential future applications of thermoelectric systems [1–10]. Thermoelectric generators (TEGs) have the capability to convert wasted exhaust heat into useful electric power in vehicles [11]. Thus, automotive companies have begun developing prototypes. Nonetheless, thermoelectric devices have not been broadly used particularly for power generation due to some of their deficiencies. Low conversion efficiencies, usually around 3–10% [1], due to the small non-dimensional figure of merit ZT value, is the major drawback of thermoelectric devices. New thermoelectric

* Corresponding author. Tel.: +1 804 503 22 60; fax: +1 804 827 70 30.

E-mail address: erturunu@vcu.edu (U. Erturun).

materials (with values of $ZT \sim 1$ and more) including thin-film superlattices, advanced bulk semiconductor alloys, and crystal structures with rattlers have been developed recently through intensive research efforts focused on enhancing efficiencies [12]. Contrary to the material level challenges, research on device-level challenges is small. This resulted as an imbalance between material and device level developments of thermoelectric devices.

Thermoelectric devices are typically consists of electrically in series and thermally in parallel connected p- and n-type thermoelectric legs, commonly fabricated with BiTe-, PbTe- or SiGe-based semiconductors. Conductor shunts, cold/hot substrates and solder joints are the other parts of a thermoelectric device. In either power generation or cooling applications, they are subjected to a temperature gradient. This causes thermal stresses in the devices due to differential thermal expansions and mismatching of thermal expansions of the bonded components [13]. Dislocations and cracks might arise due to the thermal stresses. Further, fatigue fractures may occur and finally the device may fail due to repeated thermal stresses in cyclic heating applications [14,15]. Potential failure mechanisms of thermoelectric devices were evaluated by Choi et al. [15]. More seriously, failure of even only one thermoelectric element may cause the entire device to fail since all the elements are connected electrically in series. Consequently, thermal stresses are critically important for reliability, operation life-time and expected performance of thermoelectric devices. Therefore, it is crucial to investigate developed thermal stresses in thermoelectric devices and the factors that influence them.

Researchers carried out numerical analyses to determine power generation and thermo-mechanical characteristics of thermoelectric devices and effect of geometric factors. Russel and co-workers [8,9], numerically and experimentally studied performance characterization of a thermoelectric cooling-based (TEC) thermal management system while considering parameters include geometric factor of the thermo-elements. Jang and co-workers [5,6], studied power generation performance of thermoelectric modules using numerical methods to find optimum performance parameters. Li and co-workers [13] showed that the thickness of the copper pad does not have an effect on the power output of the thermoelectric device under defined conditions. Jiang and co-workers [16] studied effect of thermoelectric leg size and variable physical parameters on power generation and conversion efficiencies of thermoelectric modules. Furthermore, Nguyen and Pochiraju [17] studied power generation performance of thermoelectric modules under transient temperature gradient conditions.

Studies on thermo-mechanical performance revealed that the maximum thermal stresses are developed at the interface between the hot side conductor and the legs of BiTe-based modules [14,18,19]. The corners of the legs are more critical through the concentrated stress levels. Researchers showed that varying leg lengths and widths changes the thermal stresses developed in the modules [19–21]. Nakatani and co-workers [22] observed that increasing conductor thickness lowers the stress caused by macroscopic deformation despite increases in the strain caused by CTE mismatches. The influence of various trapezoidal prism leg geometry configurations on thermal stress, power generation, and the device efficiency of the thermoelectric modules was also studied [23,24]. Al-Merbati and co-workers [23] showed that lower thermal stresses can be acquired by changing leg geometry and the consequence of this can enhance operation life. Investigation led by researchers showed distribution of thermal stresses in segmented thermoelectric legs [25–27]. Li and co-workers [25] observed maximum tensile stress of 180 MPa due to mismatching of thermo-mechanical properties. Consequently, thermal stresses are critically important for durability, operation life-time, and expected performance of thermoelectric devices. We agree with several

researchers [28,29], that thermoelectrics needs more device-level research. For this reason, it is crucial to investigate the factors that have impact on thermal stresses in the legs, in particular their geometry.

It is the aim of this study to investigate the possible effect of thermoelectric leg geometries on thermo-mechanical and power generation performance of thermoelectric devices. For this purpose, thermoelectric modules with various leg geometries including rectangular prism, trapezoidal prism, cylindrical and octagonal prism were modeled. Finite-element analyses were carried out for specific configurations. Power generation through an imposed steady-state temperature gradient was considered as operation mode of the thermoelectric modules. Moreover, modules with segmented thermoelectric legs were modeled considering a larger temperature gradient. Temperature distributions, magnitude of generated power outputs, conversion efficiencies, magnitude and distribution of thermal stresses were evaluated.

2. Finite element modeling

2.1. Method

In order to predict temperature distribution, power generation and thermal stresses with varying leg geometry, finite-element methods are used. Power generation and thermo-mechanical behavior of a 4-leg thermoelectric module is considered. Steady-state temperature gradients of 100 °C and 300 °C were applied since most commonly used thermoelectric devices are usually designed to operate around these temperatures. Steady-state thermal, thermoelectric, and static structural modules of ANSYS® Workbench (Academic Research, Release 14.0) were utilized to carry out temperature, power generation, and thermo-mechanical analyses, respectively. ANSYS finite element software has multi-physics coupled simulation capabilities to model and analyze thermoelectric effects with accurate solutions and is recognized by the thermoelectric device manufacturers [30].

2.2. Module geometries

Various thermoelectric leg geometries were considered. First, a 4-leg module with p- and n-type rectangular prism BiTe-based legs with dimensions of 1.4 mm × 1.4 mm × 3.0 mm was modeled. The legs were spaced with 1.0 mm distance between each other. This module was defined as the original model since thermoelectric modules are typically made of rectangular prism legs. Other modules were modeled with cylindrical and trapezoidal- and octagonal-prism leg geometries. Ease of fabrication was considered when choosing the leg geometries. Leg geometries were modeled with equal cross-sectional areas in x-y plane and heights. Cross-sectional area at mid-height was considered for the trapezoidal prism model. Modeled thermoelectric modules with their respective dimensions are shown in Fig. 1. Thicknesses of ceramic substrates, conductor pads, and solder strips are 0.8 mm, 0.15 mm, and 0.1 mm respectively. Geometries of the copper pads and solder strips were modified to match leg geometries. However, their thicknesses remained the same for all models. Segmented leg structure was considered for the temperature gradient of 300 °C. Modules with rectangular prism- and cylindrical-segmented legs were modeled. Segmented models share the same dimensions with the rectangular prism and the cylindrical non-segmented models.

2.3. Material properties

Thermoelectric modules are usually composed of p- and n-type thermoelectric legs (or so-called pins), ceramic substrates,

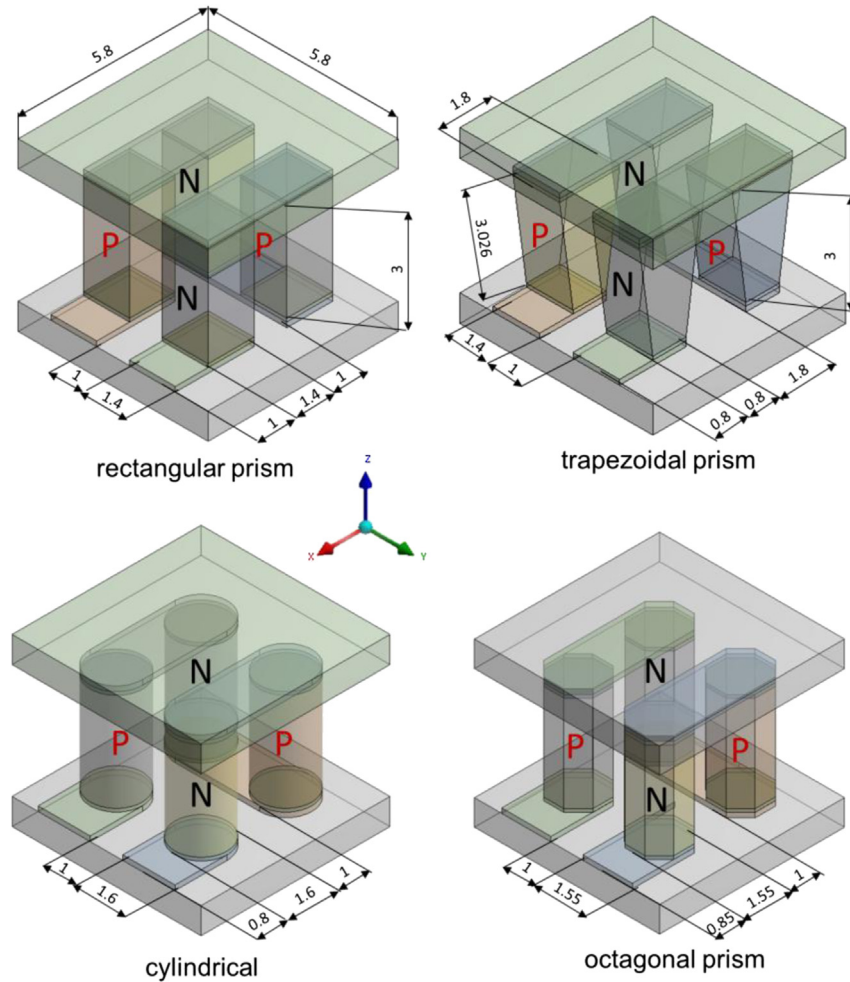


Fig. 1. Models with various leg geometries and dimensions (in mm).

conductor pads, Ni-rich diffusion barriers, and soldering strips. BiTe-based alloys are the most commonly preferred leg materials for relatively small temperature gradient applications. In our models, extruded p-type $(\text{Bi}_{0.5}\text{Sb}_{0.5})_2\text{Te}_3$ and n-type $(\text{Bi}_{0.95}\text{Sb}_{0.05})_2(\text{Te}_{0.95}\text{Se}_{0.05})_3$ alloys were preferred as the thermoelectric leg materials due to their optimal performance for our defined temperature range of 20–120 °C. In case of large temperature gradient models, segmented legs were used for optimized Seebeck voltage and maximized power output. Initial segments of the legs were modeled with the extruded BiTe-based alloys and second segments were modeled with CoSb-based (Skutterudite) p-type $\text{Ce}_{0.9}\text{Fe}_3\text{CoSb}_{12}$ and n-type $\text{Co}_4\text{Sb}_{11}\text{Ge}_{0.4}\text{Te}_{0.6}$ alloys. CoSb-based alloys were preferred due to their optimal Seebeck coefficients for high temperature applications. Temperature-dependent Seebeck coefficients of both extruded BiTe- and CoSb-based alloys are shown in Fig. 2. Other material properties of them are listed in Table 1.

Since temperatures vary across the thermoelectric device, temperature-dependent properties of the materials—including the Seebeck coefficient, thermal conductivity, coefficient of thermal expansion, and electrical resistivity—were taken into account in the finite-element models. The ANSYS Workbench analysis system supports temperature-dependent problems [31]. When a temperature-dependent property is defined, the program includes it in the solution of element matrices. The corresponding material properties in the element matrices are determined with calculation of temperatures at the center points of the elements and linear

interpolation of the material property values for these temperatures. If the calculated temperatures are beyond the extreme minimum and maximum temperatures, the program determines corresponding material properties using constant-valued extrapolations.

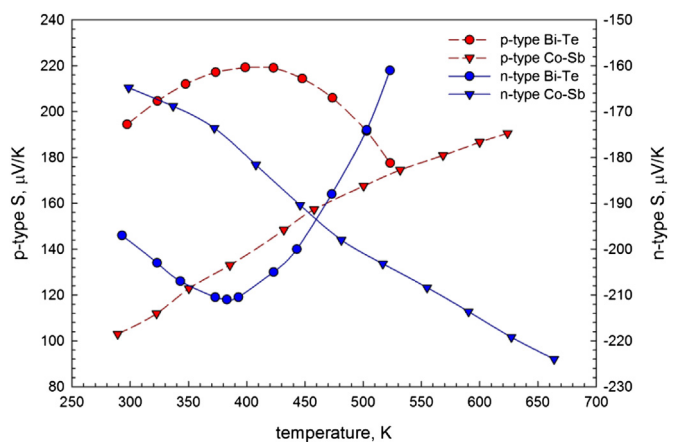


Fig. 2. Seebeck coefficients of p-type; $(\text{Bi}_{0.2}\text{Sb}_{0.8})_2\text{Te}_3$ and $\text{Ce}_{0.9}\text{Fe}_3\text{CoSb}_{12}$ alloys and n-type; $(\text{Bi}_{0.95}\text{Sb}_{0.05})_2(\text{Te}_{0.95}\text{Se}_{0.05})_3$ and $\text{Co}_4\text{Sb}_{11}\text{Ge}_{0.4}\text{Te}_{0.6}$ alloys [18,32–35].

Table 1

Properties of p-type $(\text{Bi}_{0.2}\text{Sb}_{0.8})_2\text{Te}_3$ and n-type $(\text{Bi}_{0.95}\text{Sb}_{0.05})_2(\text{Te}_{0.95}\text{Se}_{0.05})_3$ alloys [18,20,32,38,39], along with p-type $\text{Ce}_{0.9}\text{Fe}_3\text{CoSb}_{12}$ and n-type $\text{Co}_4\text{Sb}_{11}\text{Ge}_{0.4}\text{Te}_{0.6}$ alloys [27,33,34,40].

Property	p-type BiTe-based alloy	n-type BiTe-based alloy	p-type CoSb-based alloy	n-type CoSb-based alloy
d (kg/m ³)	6858	7858	7656	7539
α (10 ⁻⁶ /K)	16.8	16.8	11.5	11.5
E (GPa)			130	130
Radial	40.3	42.7		
Axial	49.7	51.0		
v	0.28	0.28	0.23	0.23
λ (W/m K)	1.22–5.24 (300–500 K)	1.78–3.50 (300–500 K)	1.87–1.77 (300–600 K)	4.49–3.20 (300–600 K)
ρ ($\mu\Omega \text{ m}$)	13.8–25.0 (300–500 K)	9.8–14.9 (300–500 K)	10.43–12.65 (300–600 K)	11.07–13.87 (300–600 K)

Copper alloy was preferred as the conductor material due to its high electrical and thermal conductivity. In order to join the legs and conductor pads two different soldering alloy were used. 63Sn–37Pb alloy was preferred for the small temperature gradient models. For the large temperature gradient models, 92.5Pb–5Sn–2.5Ag alloy was preferred due to its superior electrical, thermal, and mechanical properties. Moreover durability of 92.5Pb–5Sn–2.5Ag alloy is higher than 63Sn–37Pb alloy at high temperatures. In order to provide mechanical integrity of the module, Al_2O_3 ceramic substrates were preferred. Material properties of the conductors, soldering alloy, and ceramic substrates are listed in Table 2. Temperature dependencies of some material properties including thermal and electrical conductivities were considered in the simulations. Thin Ni-rich diffusion barriers were not modeled since their effect on thermo-mechanical behavior of the thermoelectric module is negligible due to their very small thicknesses, usually 4 μm , compared to thicknesses of 100 μm for the solder and 150 μm for the conductor parts.

Research in the literature revealed that thermal stresses in the thermoelectric legs can be significantly lowered due to the elastic and plastic deformation of the conductor and soldering materials [18,20,27]. Particularly soldering alloys have an important role to reduce the stress levels in the legs since their yield strength is lower than the strength of leg material. Clin et al. [18] concluded that stresses in the legs could be two or three times higher if the plastic deformation of the soldering alloy is not considered. Thus, elasto-plastic behavior of the conductor and the soldering alloys is considered in our finite-element models. Bilinear kinematic hardening is preferred between the yield and the ultimate tensile stresses of the Cu conductor and the 63Sn–37Pb solder. Elongation, yield stresses, and ultimate tensile stresses of the Cu

Table 2

Properties of Al_2O_3 (A4, 99.7%), Cu-based, 63Sn–37Pb, and 92.5Pb–5Sn–2.5Ag alloys [20,41–48].

Property	Al_2O_3 substrate	Cu-based conductor	63Sn–37Pb solder	92.5Pb–5Sn–2.5Ag solder
d (kg/m ³)	3970	8940	8420	11300
α (10 ⁻⁶ /K)	4.89–6.68 (223–600 K)	16.7–17.6 (223–583 K)	24	29
E (GPa)	380–366 (293–600 K)	119–100 (273–600 K)	36–12 (273–423 K)	23–15 (300–600 K)
v	0.26	0.31	0.40	0.44
σ_y (MPa)	70	20		
σ_{UTS} (MPa)	250	40		
%EL	69	40		
λ (W/m K)	37.2–17.2 (293–600 K)	398–382 (293–600 K)	53–46 (273–423 K)	35
ρ ($\mu\Omega \cdot \text{m}$)	1×10^{18} (300–600 K)	0.18–0.38 (293–473 K)	0.12–0.23 (300–600 K)	0.2

Table 3

Anand viscoplasticity model constants of 92.5Pb–5Sn–2.5Ag alloy [37].

S_0 (MPa)	Q/\bar{R} (K)	D_0 (sec ⁻¹)	ξ	m	h_0 (MPa)	\hat{S} (MPa)	n	a
33.07	11024	1.052(10 ⁵)	7	0.241	1432	41.63	0.002	1.3

conductor and the 63Sn–37Pb solder are shown in Table 2. Anand viscoplasticity is a commonly used model in finite-element simulations to simulate elasto-plastic behavior of 92.5Pb–5Sn–2.5Ag solders [36,37]. In our large temperature gradient (300 °C) models, Anand viscoplasticity was applied since it is a verified model for deformation behavior of 92.5Pb–5Sn–2.5Ag solders at high temperatures. The model constants for 92.5Pb–5Sn–2.5Ag alloy are listed in Table 3.

2.4. Simulation parameters and meshing

Thermoelectric power generation was considered while defining simulation parameters for the models. In case of small temperature gradient models, steady state temperature values of 120 °C and 20 °C were imposed on the hot and cold sides of the module, respectively. In case of large temperature gradient models, imposed temperature values were 320 °C and 20 °C. Environmental temperature was assumed to be 20 °C for all models. Seebeck electric potentials were calculated analytically using the formula below

$$V = S(T_H - T_C) \quad (1)$$

where S is Seebeck coefficient, T_H is hot side and T_C is cold side temperature. Calculated Seebeck electric potentials for the small and large temperature gradient models were 45 mV and 108 mV, respectively. These electric potential values are considered as high electric potentials and applied to the p-type conductor pads. Low electric potentials are defined as 0 mV for the n-type conductor pads. Air convection with the coefficient of 10 W/m² °C is assumed and applied to the outer surfaces of the modules. The modules are mechanically unconstrained and remain free-standing during the simulations. Medium size meshing is preferred using the automatic mesh feature of ANSYS. Defined parameters and meshed models are shown in Fig. 3(a) and (b) for the temperature gradient of 100 °C and 300 °C cases, respectively.

In order to establish mesh convergence, the results of a critical parameter (stress, strain, or deflection) in a specific location is being plotted against a measure of mesh density. Simulation parameters illustrated in Fig. 3(a) are used. As shown in Fig. 4, the equivalent stress results of a very critical point—a hot side corner of a rectangular prism leg—was plotted against the number of nodes after eight convergence runs. This plot can be used to indicate when the convergence is achieved. The model converges above 46×10^3 nodes when the stress value difference between the runs remains less than 0.7%. According to these results, the finite-element models used in this study converge since their mesh patterns contain at least 75×10^3 nodes.

2.5. Model verification method

In order to validate our finite-element model, numerical results were compared with experimental measurements. Height differences ΔZ between a corner and the center point on the hot side surface of a commercially available 40 × 40 mm² thermoelectric module, Kryotherm TB-127-1.4-1.5, were experimentally measured for different temperature gradients. Total thickness of the module is 3.9 mm and consists of p-type $(\text{Bi}_{0.5}\text{Sb}_{0.5})_2\text{Te}_3$ and n-type

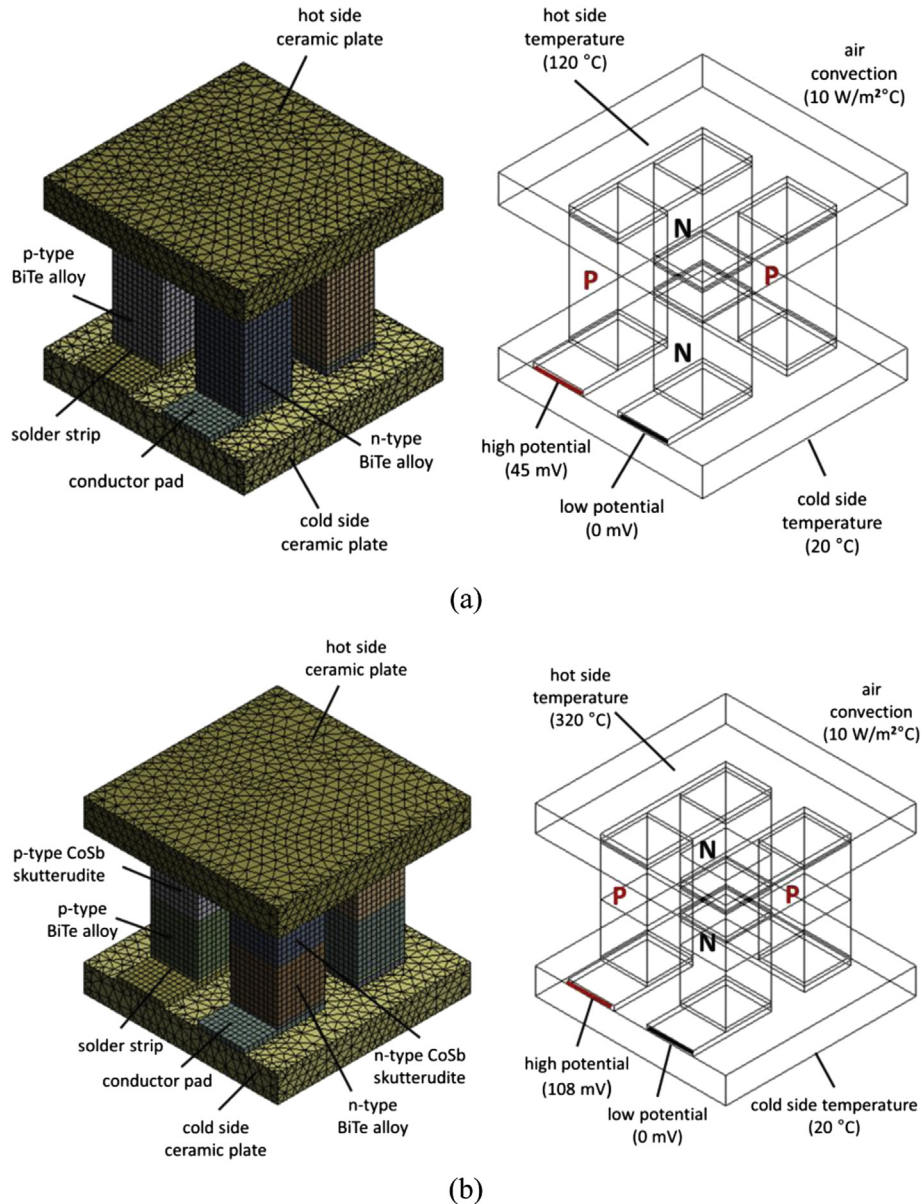


Fig. 3. Finite-element models and simulation parameters for the temperature gradient of (a) 100 °C and (b) 300 °C.

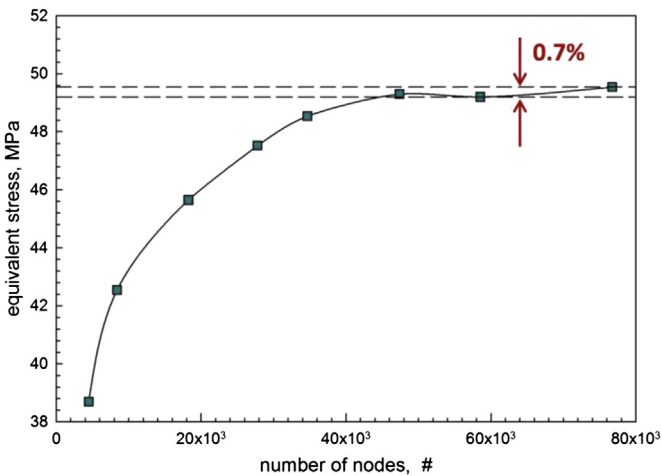


Fig. 4. Convergence of the predicted equivalent stresses in a rectangular prism leg as a function of the total number of nodes in its mesh pattern.

($\text{Bi0.95Sb0.05})_2(\text{Te0.95Se0.05})_3$ legs (total number of 256) with a height of 1.5 mm and a width of 1.4 mm. An experimental setup consists of an Ambios XP-1 stylus profiler, a Fluke 52 K/J digital thermometer, type K thermocouples, a laser thermometer and a GW Insteck PSP405 programmable DC power supply was used. The profiler has maximum vertical range of 400 μm and vertical resolution of 15 \AA at 100 μm . In order to measure profiles: (1) the module was heated by applying certain DC voltages and currents (and thereby obtaining the Peltier effect), (2) temperatures and corresponding power inputs were recorded, (3) thermocouples were removed and the profiler probe was positioned on the center—starting point—of the hot side surface, (4) profiles were measured by running the stylus profiler for each temperature gradient while temperatures were monitored with the non-contact infrared thermometer and (5) ΔZ between the center and corner points were calculated using the profile data. Profiler setup and measured ΔZ are illustrated through Fig. 5(a)–(c).

To predict the height differences, thermo-mechanical finite element analyses of a quarter model—since the module is quasi-

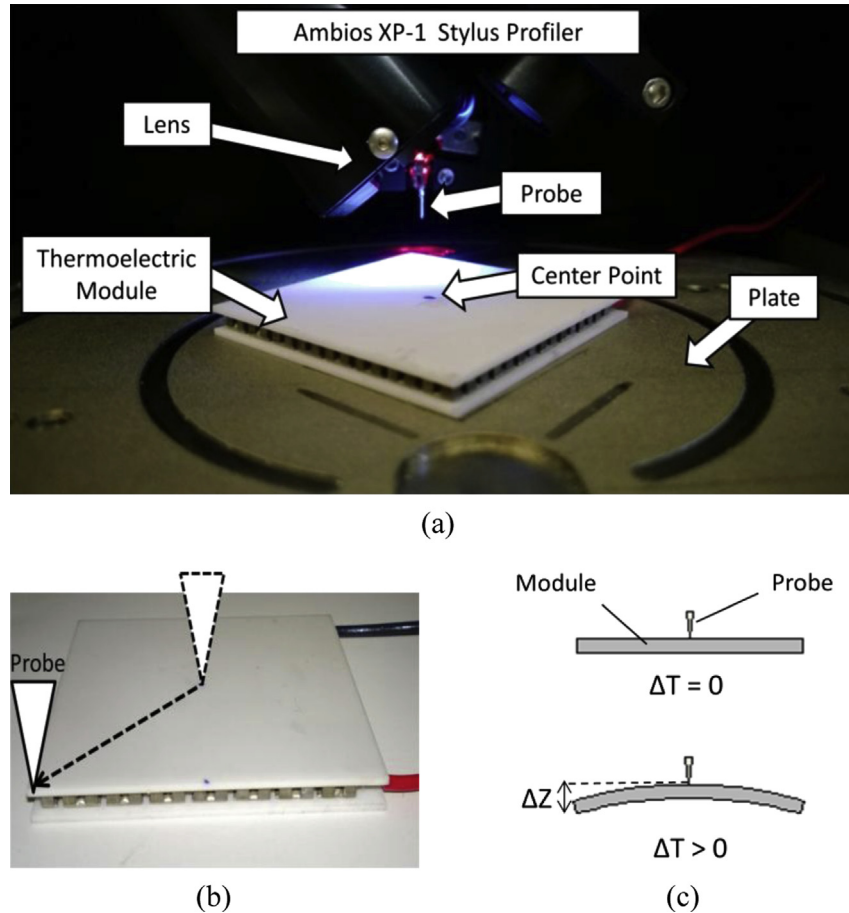


Fig. 5. Profile measurements; (a) inside of the stylus profiler, (b) direction of the probe and (c) measured height difference (ΔZ).

symmetric—were carried out. Our 4-leg finite-element model showed in Fig. 3(a) was modified to a quasi-symmetric 64-leg model has matching materials and dimensions of the quarter of the Kryotherm device. Thermal and mechanical material properties of p- and n-type BiTe-based legs, 92.5Pb–5Sn–2.5Ag solder, Cu-based conductor and Al₂O₃ substrate, listed in Tables 1 and 2, were used.

3. Results and discussions

3.1. Temperature analysis

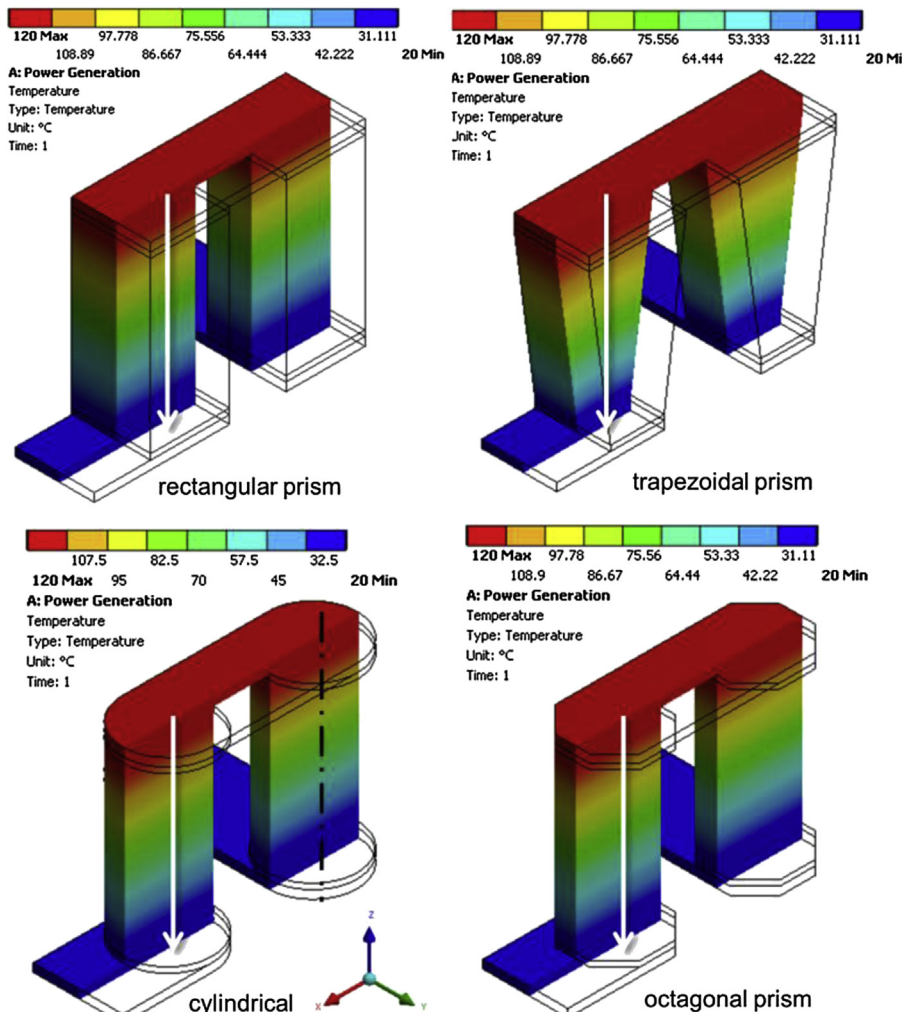
Temperature distributions of the thermoelectric modules were calculated through steady-state thermal analysis. Imposed temperature gradient causes heat flow through entire module. For temperature gradient of 100 °C, temperature distributions of a thermoelectric element (coupled p- and n-type legs) with conductor pads and soldering strips of each model are presented in Fig. 6(a). Other parts of the thermoelectric modules are hidden in the figure for only visualization purposes. In addition, temperature distributions along the defined paths in the z-axis shown in Fig. 6(a) are plotted and presented in Fig. 6(b). Temperature decays significantly along the z-axis between the hot and cold side while it remains almost equal along the x- and y-axis for the all models as shown in Fig. 6(b). All models except the trapezoidal prism presented fairly similar and linear temperature profile changes along the z-axis path; trapezoidal prism legs presented slightly different temperature decays than the other legs. This result is a

consequence of various cross-sectional areas of the trapezoidal prism legs.

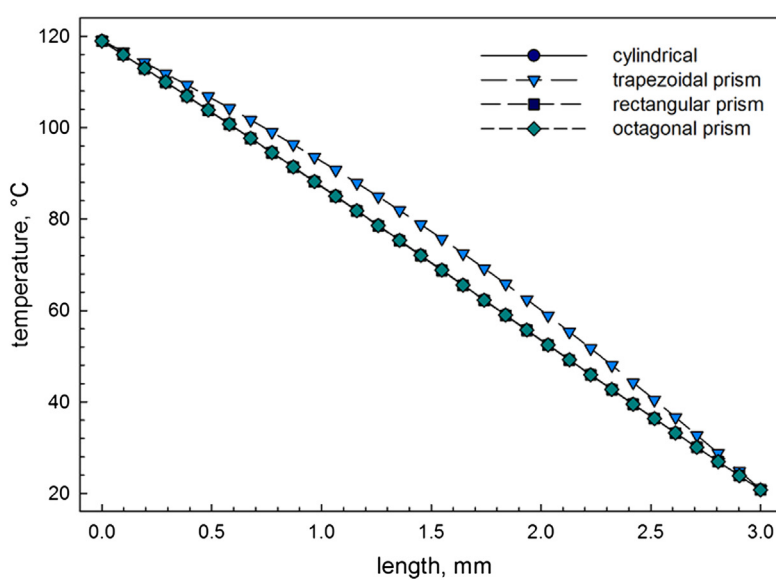
Temperature distributions of the segmented models for the temperature gradient of 300 °C are shown in Fig. 7(a) and (b). Rectangular prism- and cylindrical-segmented legs presented a fairly similar temperature distribution trend. Temperature decays along the z-axis were not linear in this case as shown in Fig. 7(b). Noticeable changes in the slope of the profiles can be clearly seen above the mid-height of the legs. This non-linearity occurs due to the different thermal conductivities of BiTe- and CoSb-based alloys. Overall, thermal analysis results show that temperature distributions were slightly affected by changing thermoelectric leg geometries.

3.2. Power generation analysis

In order to evaluate the effect of thermoelectric leg geometries on the power generation performance of thermoelectric modules, finite-element thermoelectric analyses were performed on rectangular-, trapezoidal-, octagonal-prism, and cylindrical models for the temperature gradient of 100 °C. Applied temperature gradients generate electric current flow through p- and n-type legs in series. Total current densities shown as contours in Fig. 8 present the current flows in various leg geometries. Electric current and absorbed heat magnitudes were obtained as finite-element analysis results. Generated power outputs and conversion efficiencies were analytically calculated applying the numerical results, the electric current and absorbed heat, in the equations below



(a)



(b)

Fig. 6. Temperature distributions in the legs (a) as nephogram and (b) along the paths for the temperature gradient of 100 °C.

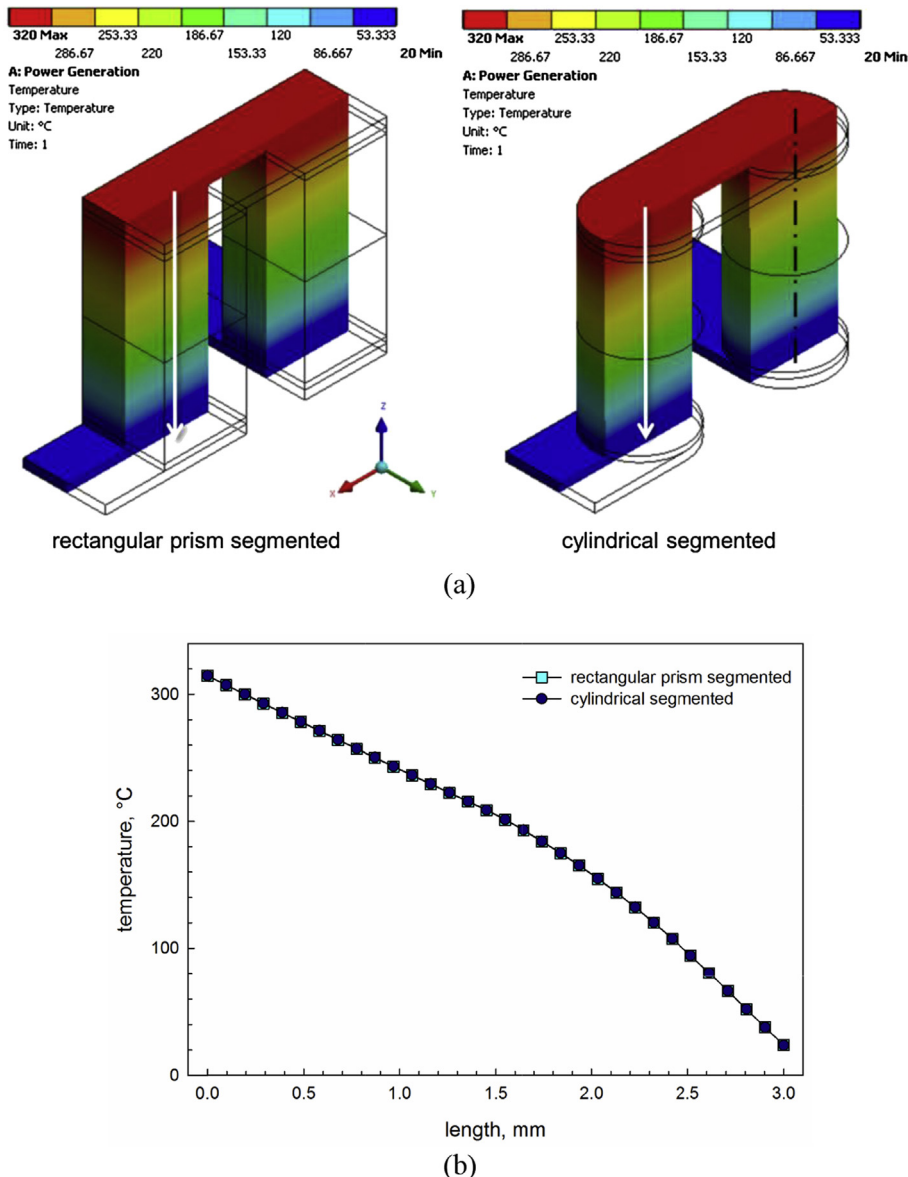


Fig. 7. Temperature distribution in the segmented legs (a) as nephogram and (b) along the paths for the temperature gradient of 300 °C.

$$P = N \left[S(T_H - T_C)I - I^2 R \right] \quad (2)$$

$$R = \frac{L}{A} (\rho_n + \rho_p) \quad (3)$$

$$\eta = \frac{P}{Q_H} \quad (4)$$

where P is output power, N is number of thermoelectric elements in the module (in our models; $N = 2$), S is Seebeck coefficient, T_H is hot side temperature, T_C is cold side temperature, I is electric current, R is combined internal electrical resistance for the p- and n-type thermoelectric legs, A and L are cross-sectional area and length of the legs, ρ_p and ρ_n are electrical volume resistivity for the p- and n-type legs respectively, η is conversion efficiency and Q_H is absorbed heat. Joule heating $I^2 R$ due to internal electrical resistance of

thermoelectric materials [49] was considered in the power calculation. Generated electric current I and absorbed heat Q_H as finite-element analysis results and calculated conversion efficiencies η are shown in Fig. 9. Calculated power outputs for rectangular prism, trapezoidal prism, cylindrical, and octagonal prism models were 18.31 mW, 17.64 mW, 18.85 mW, and 18.54 mW, respectively. Although the electric current flows were slightly affected by geometrical differences, the changes in the power outputs remained very small. This result was expected since the parameters including Seebeck coefficients, temperature gradients, and heights of the thermoelectric legs were the same for all models. Disparities in power output and efficiency values of the trapezoidal prism model were consequence of its various cross-sectional leg areas.

In order to calculate electrical current and absorbed heat for the temperature gradient of 300 °C, numerical thermoelectric analyses were performed on rectangular prism- and cylindrical-segmented models. Power outputs and conversion efficiencies were calculated using finite-element analysis results (I and Q_H) and equations (2)–(4). Generated electric current I , absorbed heat Q_H and

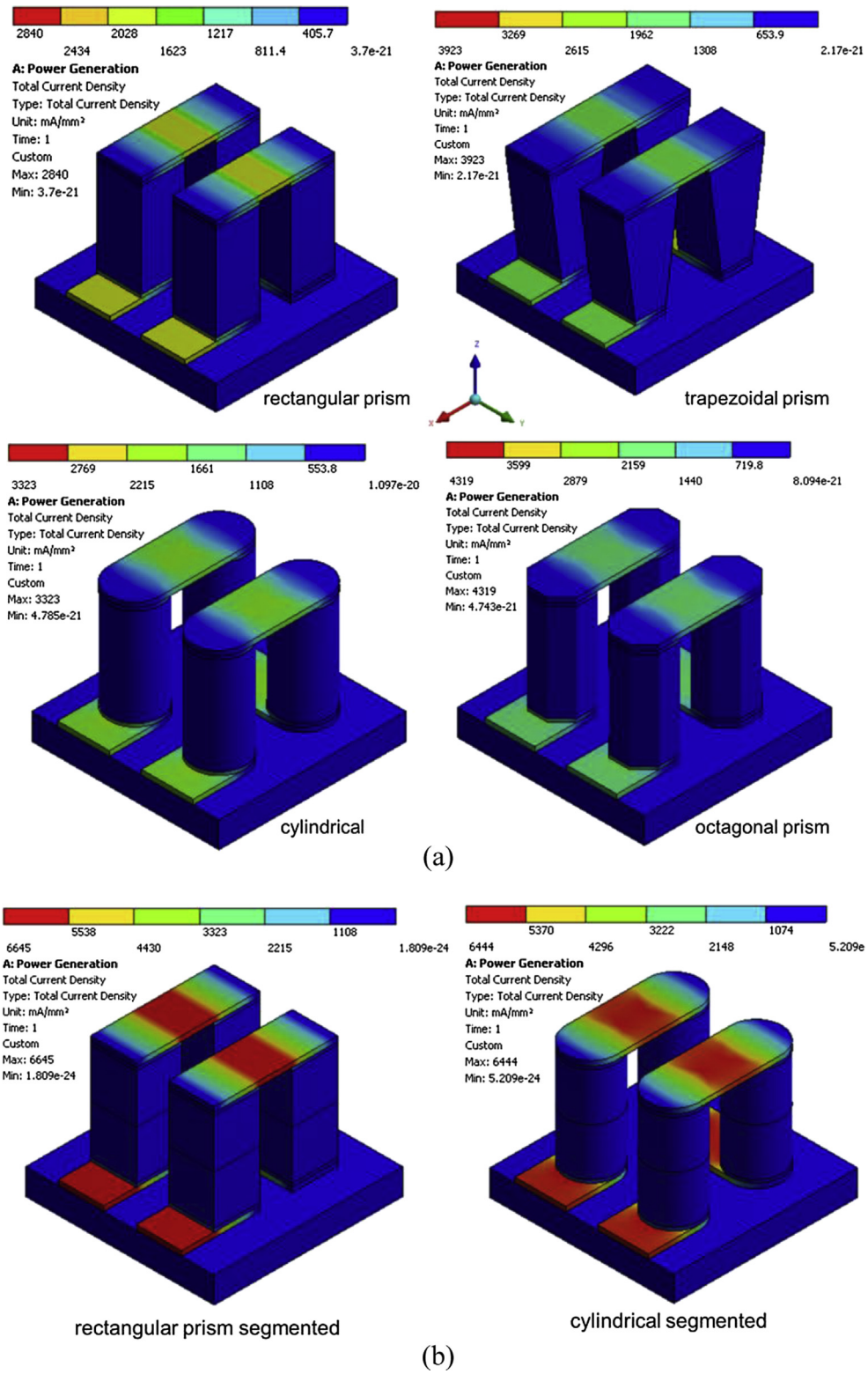


Fig. 8. Total current densities for the temperature gradients of (a) 100 °C and (b) 300 °C.

calculated conversion efficiencies η are shown in Fig. 9 for the temperature gradient of 300 °C. Calculated power outputs for rectangular prism-segmented and cylindrical-segmented models were 143.6 mW and 143.7 mW respectively. It can be seen that, power outputs were almost 8 times greater and conversion efficiencies were almost 2 times greater than those of the temperature gradient

of 100 °C case. This is as a result of higher Seebeck coefficients in segmented models as well as larger temperature gradients. Performance difference between rectangular prism-segmented and cylindrical-segmented models remained negligible. It is noted that, optimization of the power output performance or conversion efficiency is not the aim of this study.

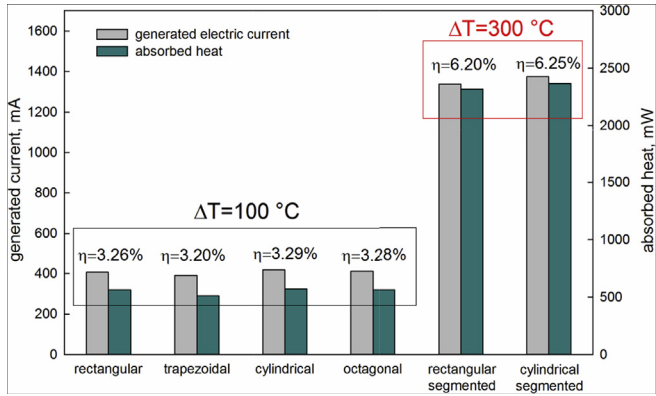


Fig. 9. Predicted electric current, absorbed heat, and calculated conversion efficiencies.

3.3. Thermo-mechanical analysis

In order to evaluate the impact of various thermoelectric leg geometries on thermo-mechanical performance, thermal stresses developed in the legs due to temperature gradients and thermal expansion mismatches were analyzed for steady-state conditions. Coupling temperature and static-structural analyses compose thermo-mechanical analysis. Temperature distributions obtained from the thermal analysis were applied as load for static-structural analyses. Thermal stresses were developed in the legs due to expansion of the hot side ceramic substrate while the cold side obstructs and thermal expansion mismatches between the materials constituting the thermoelectric module. Thermal stress levels were calculated in terms of equivalent stresses σ_v (so-called von Mises stresses). Equivalent stress is preferred since it is an average scalar stress value computed from the second deviatoric stress components σ_{ij} , cauchy or so-called true stress tensors as formulated below:

$$\sigma_v = \sqrt{\frac{(\sigma_{11} - \sigma_{22})^2 + (\sigma_{22} - \sigma_{33})^2 + (\sigma_{33} - \sigma_{11})^2 + 6(\sigma_{12}^2 + \sigma_{23}^2 + \sigma_{31}^2)}{2}} \quad (5)$$

Distribution and maximum values of calculated equivalent stresses in the legs for rectangular prism, trapezoidal prism, cylindrical, and octagonal prism models are shown in Fig. 10(a) for temperature gradient of 100 °C. As expected, the maximum stress zones were developed in the legs on the hot side of the module. This is due to higher thermal expansions and larger CTE differences between the materials on the hot side. Maximum stresses occur on the hot side corner of the legs (for cylindrical models on the edges) and their values for rectangular prism, trapezoidal prism, cylindrical, and octagonal prism models were 49.9 MPa, 41.5 MPa, 43.3 MPa, and 47.8 MPa, respectively. In order to evaluate variation of the stress values from one leg to the other in different directions, stress paths taking the maximum stress node as starting point were constructed. Equivalent stress distributions along the paths in the x-, y-, and z-axis are illustrated in Fig. 10(b), (c) and (d). We observe that the stress values were smaller in the middle section and larger on the edge of the legs. Along the path of x-axis, stresses distributed more uniformly in the trapezoidal prism legs compared to the others. This can be attributed to the longer hot side edges (1.8 mm compared to 1.4 mm of the rectangular prism leg) of the trapezoidal prism legs. Along the path of z-axis, thermal stress levels increase closer to the mid-height sector along with the hot and cold side surfaces. Stress values along the paths of y- and z-axis are smaller in

the cylindrical and the octagonal prism legs compared to the others. Maximum principal stresses in the legs were also calculated: 40.5 MPa, 42.5 MPa, 33.3 MPa, and 35.7 MPa for rectangular prism, trapezoidal prism, cylindrical, and octagonal prism models, respectively. These results show that changing leg geometry can significantly reduce and redistribute thermal stresses in the thermoelectric legs. Cylindrical or trapezoidal prism legs can be preferred over the other leg geometries due to their small stress levels and ease of fabrication (particularly with respect to the dicing process) compared to the octagonal prism models. To fabricate a typical thermoelectric device, thermoelectric legs are diced in the desired dimensions from the plated p- and n-type semiconductor wafers using regular cutting saws or Electrostatic Discharge Machining (EDM). Copper conductor pads and Al₂O₃ ceramic substrates are also diced to the proposed dimensions.

Predicted maximum plastic strains on the conductor pads were 0.33%, 0.32%, 0.24%, and 0.25% for rectangular prism, trapezoidal prism, cylindrical, and octagonal prism models, respectively. Maximum plastic strains on the soldering strips were 0.57%, 0.67%, 0.65%, and 0.74% for rectangular prism, trapezoidal prism, cylindrical, and octagonal prism models, respectively. These values are much smaller than the plastic extensibilities of 69% for the copper conductor and 40% for 63Sn–37Pb soldering alloys shown in Table 2. It is clear that both conductor pads and soldering strips were plastically deformed, but they were still in the safe zone and will not fail for the defined conditions. In our previous thermo-mechanical analysis of thermoelectric modules [50], only elastic behavior of the soldering and conductor alloys (zero plastic deformation) was taken into account. The maximum equivalent stress of 129 MPa was calculated in the rectangular prism thermoelectric legs for the temperature gradient of 138 °C. In the present study, the maximum equivalent stress of 49.9 MPa was calculated in the rectangular prism legs for the temperature gradient of 100 °C. This decrease in the stress levels occurred due to the elastic and plastic deformations of the conductor and soldering alloys. Elasto-plastic behavior of the conductor and soldering alloys is more appropriate to represent the stress levels compare to the linear elastic behavior.

In case of temperature gradient of 300 °C, developed thermal stresses in the legs of the rectangular prism- and cylindrical-segmented models were analyzed. Levels and distribution of calculated equivalent stresses are shown in Fig. 11(a). Maximum thermal stress magnitudes were smaller in the cylindrical segmented legs compare to the stresses in the rectangular prism segmented legs. In the rectangular prism segmented model, a calculated maximum equivalent stress of 94.2 MPa was occurred between the CoSb- and BiTe-based segments. In the cylindrical segmented model, maximum equivalent stress of 85.7 MPa was occurred on the hot side edge of the CoSb-based segment. Distribution of the stresses is illustrated by using the paths shown in Fig. 11(a) and the profiles along these paths in Fig. 11(b), (c), and (d). Stress evolution of the segmented legs displays distinctive trends compared to the non-segmented models. Significant changes in the stress magnitudes and distributions were observed in the joints of the segments as shown along the path of z-axis in Fig. 11(d). In the segmented models high stress levels occur between the segments due to the thermal expansion differences between BiTe- and CoSb-based alloys. It is noted that different soldering alloy and plasticity models were used in the segmented models. This made impact on stress trends on the hot side of the legs as shown along the path y_{top} in Fig. 11(c). Maximum plastic strains of 1% and 3.4% were developed in the conductor pads and soldering strips of the rectangular prism- segmented model. They were 0.93% and 0.64%, respectively for the cylindrical-segmented model. Overall, increases in thermal stresses magnitude (due to

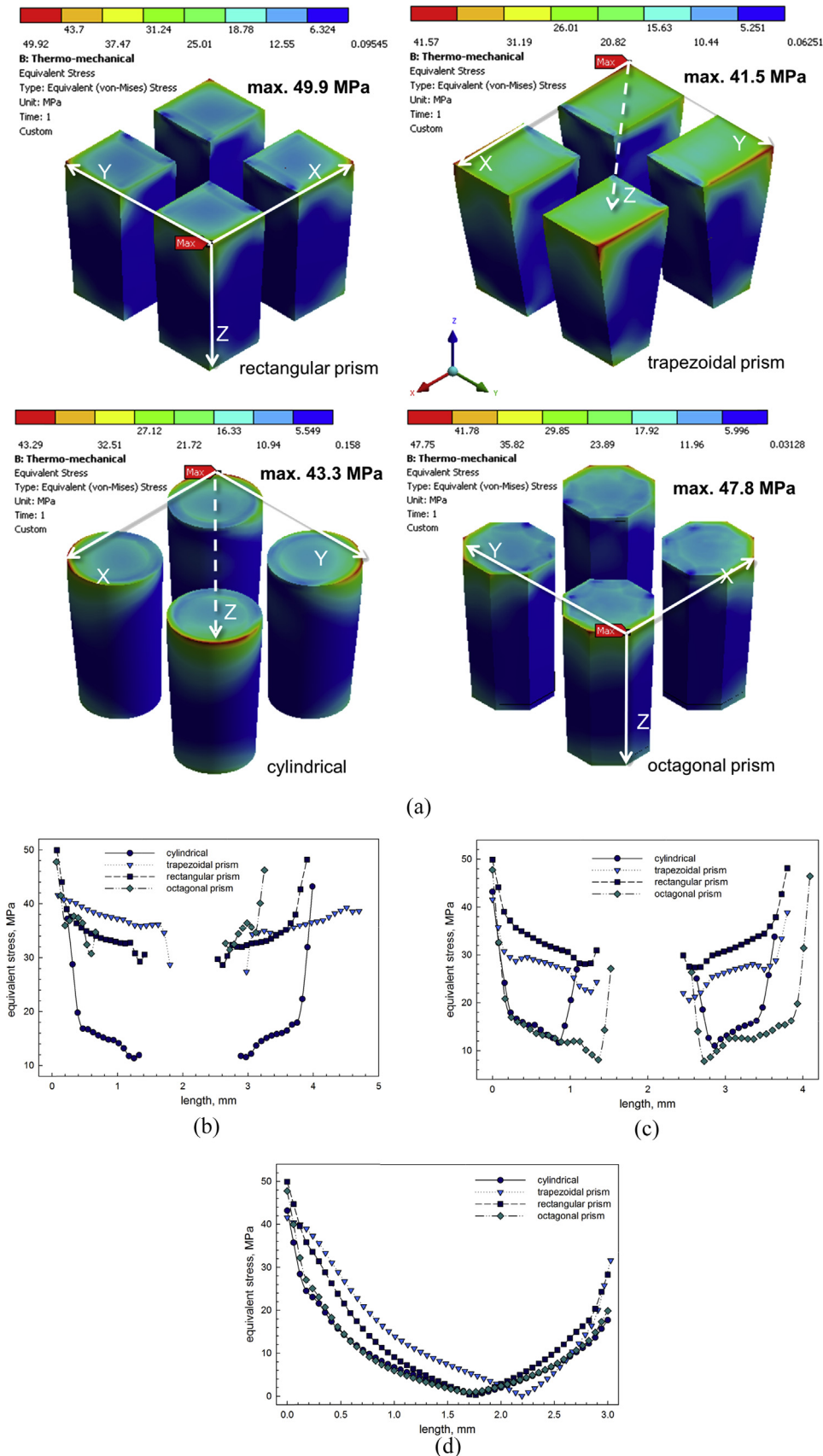


Fig. 10. Magnitude and distribution of maximum equivalent stresses in the legs; (a) as nephogram and along the (b) x-, (c) y-, and (d) z-axis paths for the temperature gradient of 100 °C.

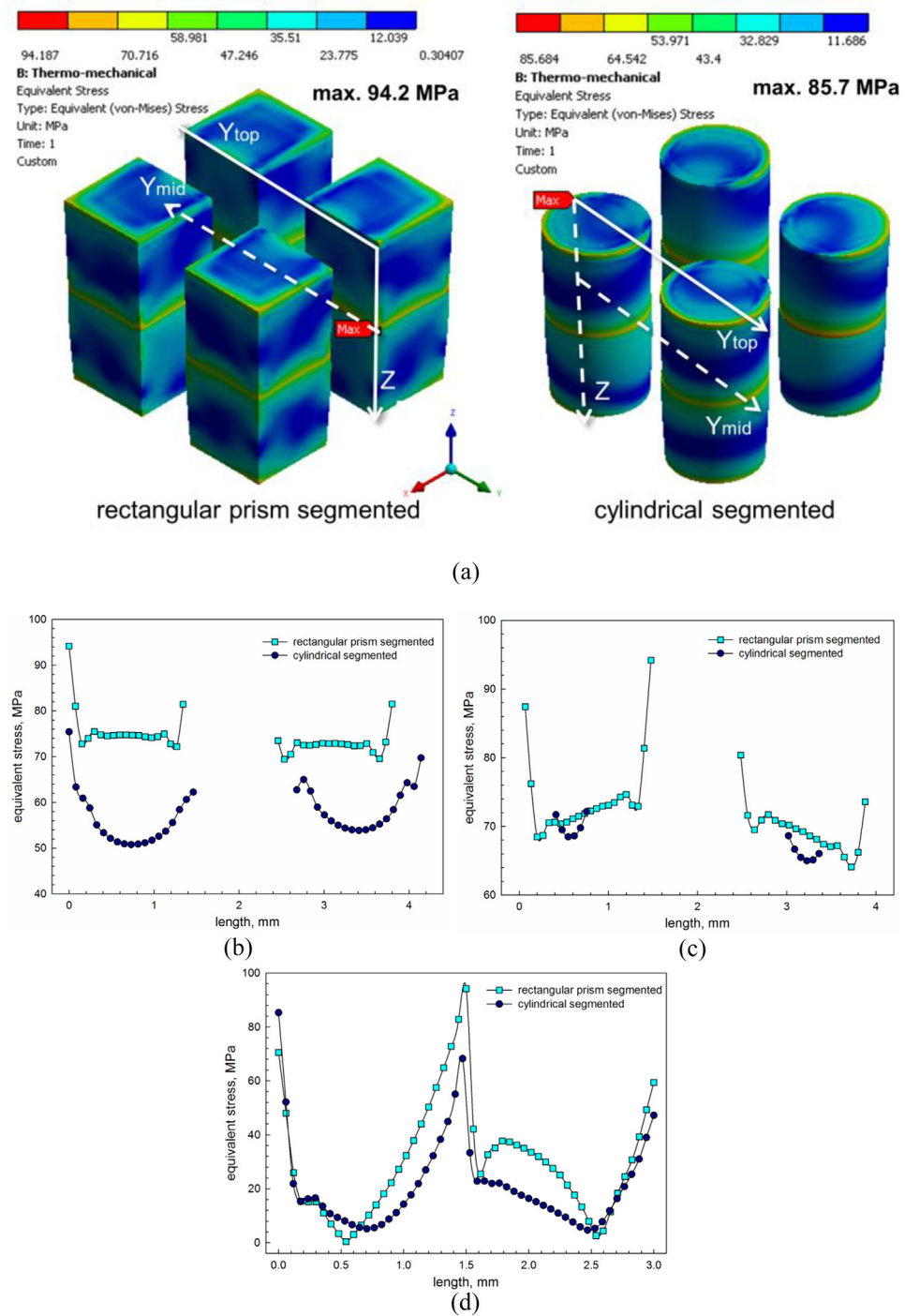


Fig. 11. Maximum equivalent stresses in the segmented legs; (a) as nephogram and along the (b) y_{mid} -, (c) y_{top} -, and (d) z -axis paths for the temperature gradient of 300 °C.

larger temperature gradients) and distinctive stress distributions were observed in the segmented legs.

3.4. Verification results

Experimental profile measurements and numerical simulations were performed using the temperatures, shown in Table 4. Height differences ΔZ between the center point and the corner of the hot side of the module were experimentally measured for the defined temperatures. Corresponding ΔZ values were numerically

Table 4
Measured hot and cold side temperatures of the Kryotherm thermoelectric device.

#	T_H (°C)	T_C (°C)	ΔT (°C)
1	49	32	17
2	61	40	21
3	70	44	26
4	80	48	32
5	90	63	27
6	100	73	27
7	110	80	30
8	122	91	31

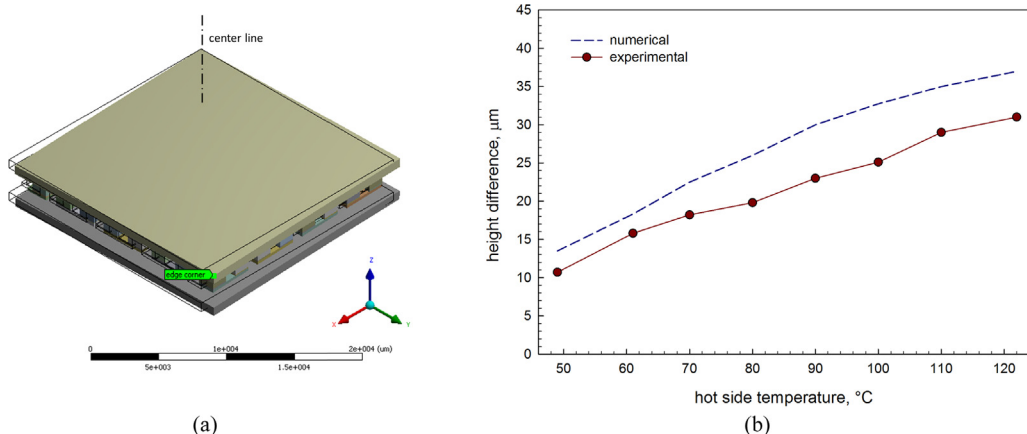


Fig. 12. Results show (a) numerical simulation of deflection and (b) comparison of experimental and numerical ΔZ values.

predicted using the 64-leg quasi-symmetric model for the same temperatures and the boundary conditions. Results of analysis—temperature distributions and mechanical deformations—are shown in Fig. 12. Moreover, our numerical results were also compared to results of a study in the literature. Turenne et al. [20] modeled a Kryotherm TB-127-1.4-1.50 thermoelectric device and predicted a ΔZ of 73 μm between the center and the external corner of the hot side for the temperature gradient of 100 $^{\circ}\text{C}$. They experimentally measured a corresponding ΔZ of 63 μm using a laser profiler. In our finite-element model, a ΔZ of 73.74 μm was predicted for the temperature gradient of 100 $^{\circ}\text{C}$ under the same boundary conditions with their simulations. These results validate our finite-element model for the thermo-mechanical analysis.

4. Conclusion

Effect of thermoelectric leg geometries on power generation and thermo-mechanical performance of thermoelectric devices was evaluated utilizing numerical methods. Rectangular prism, trapezoidal prism, cylindrical, and octagonal prism leg geometries and steady-state temperature gradients of 100 $^{\circ}\text{C}$ and 300 $^{\circ}\text{C}$ were considered. Thermoelectric modules with BiTe-based non-segmented and BiTe/CoSb-based segmented legs were modeled. Temperature-dependent material properties and stress relaxation mechanisms due to elasto-plastic behavior were considered in the finite-element models. The following conclusions were reached: (1) Changes in temperature distributions, power outputs, and conversion efficiencies were limited for various leg geometries. (2) Elastic and plastic deformations of the soldering and conductor alloys helped to decrease the stress levels in the legs. (3) Changes in thermal stress distributions and magnitude of maximum equivalent stresses were significant for various leg geometries. Maximum equivalent stresses in the rectangular prism and cylindrical legs were 49.9 MPa and 43.3 MPa, respectively for the temperature gradient of 100 $^{\circ}\text{C}$. (4) Maximum equivalent stresses were 94.2 MPa and 85.7 MPa in the rectangular prism-segmented and cylindrical-segmented legs for the temperature gradient of 300 $^{\circ}\text{C}$. In the segmented models, high stresses were occurred also between the segments along with the hot sides of the legs. (5) It is clear that in both non-segmented and segmented models, leg geometries have a significant effect on the thermo-mechanical performance of thermoelectric devices. In order to reduce thermal stresses developed in thermoelectric devices, varying thermoelectric leg geometry can be considered as a factor.

Nomenclature

S	Seebeck coefficient, V/K
V	Seebeck voltage, V
Q_H	hot side heat absorbed, W
P	useful output power, W
N	number of thermoelectric elements, —
R	electrical resistance for a thermoelectric element, $\mu\Omega$
L	length of a thermoelectric leg, m
A	cross-sectional area of a thermoelectric leg, m^2
I	electric current, A
T_H	hot side temperature, K
T_C	cold side temperature, K
d	density, kg/m^3
α	coefficient of thermal expansion, K^{-1}
λ	thermal conductivity, $\text{W}/\text{m K}$
E	modulus of elasticity, GPa
ν	poison's ratio, —
σ_y	yield strength, MPa
σ_{UTS}	ultimate tensile strength, MPa
$\%EL$	percent elongation at yield, —
ρ	electrical volume resistivity, $\mu\Omega \cdot \text{m}$
S_0	initial value of deformation resistance, MPa
Q	activation energy, ev
R	ideal gas constant, $\text{J}/\text{kg K}$
D_0	pre-exponential factor, sec^{-1}
ξ	multiplier of stress, —
m	strain rate sensitivity of stress, —
h_0	hardening/softening constant, MPa
\hat{S}	coefficient for deformation resistance saturation, MPa
n	strain rate sensitivity of deformation resistance, —
a	strain rate sensitivity of hardening or softening, —
η	efficiency, —
σ_{ij}	stress tensor components, MPa
σ_v	equivalent (von-Mises) stress, MPa
ΔZ	height difference, μm

References

- [1] X.F. Zheng, Y.Y. Yan, K. Simpson, A potential candidate for the sustainable and reliable domestic energy generation—Thermoelectric cogeneration system, *Appl. Therm. Eng.* 53 (2) (2013) 305–311.
- [2] S.B. Riffat, X. Ma, Thermoelectrics: a review of present and potential applications, *Appl. Therm. Eng.* 23 (8) (2003) 913–935.
- [3] Y.-H. Cheng, W.-K. Lin, Geometric optimization of thermoelectric coolers in a confined volume using genetic algorithms, *Appl. Therm. Eng.* 25 (17) (2005) 2983–2997.

[4] H.-S. Choi, S. Yun, K. Whang, Development of a temperature-controlled car-seat system utilizing thermoelectric device, *Appl. Therm. Eng.* 27 (17) (2007) 2841–2849.

[5] J.-Y. Jang, Y.-C. Tsai, Y.-C. Huang, Optimal design of the heat spreader applied thermoelectric module for waste heat recovery, *Adv. Sci. Lett.* 14 (1) (2012) 253–257.

[6] J.-Y. Jang, Y.-C. Tsai, Optimization of thermoelectric generator module spacing and spreader thickness used in a waste heat recovery system, *Appl. Therm. Eng.* 51 (1) (2013) 677–689.

[7] M. Lossec, B. Multon, H. Ben Ahmed, Sizing optimization of a thermoelectric generator set with heatsink for harvesting human body heat, *Energy Convers. Manag.* 68 (2013) 260–265.

[8] M.K. Russel, D. Ewing, C.Y. Ching, Numerical and experimental study of a hybrid thermoelectric cooler thermal management system for electronic cooling, *Compon. Packag. Manuf. Technol. IEEE Trans.* 2 (10) (2012) 1608–1616.

[9] M.K. Russel, D. Ewing, C.Y. Ching, Characterization of a thermoelectric cooler based thermal management system under different operating conditions, *Appl. Therm. Eng.* 50 (1) (2013) 652–659.

[10] J. Gao, K. Sun, L. Ni, M. Chen, Z. Kang, L. Zhang, Y. Xing, J. Zhang, A thermoelectric generation system and its power electronics stage, *J. Electron. Mater.* 41 (6) (2012) 1043–1050.

[11] J. Yang, F.R. Stabler, Automotive applications of thermoelectric materials, *J. Electron. Mater.* 38 (7) (2009) 1245–1251.

[12] T.M. Tritt, Thermoelectric phenomena, materials, and applications, *Annu. Rev. Mater. Res.* 41 (2011) 433–448.

[13] S.-L. Li, C.-K. Liu, C.-Y. Hsu, M.-C. Hsieh, M.-J. Dai, S.-T. Wu, Thermo-mechanical analysis of thermoelectric modules, in: *Microsystems Packaging Assembly and Circuits Technology Conference (IMPACT)*, 2010 5th International, 2010, pp. 1–4.

[14] H. Kaibe, I. Aoyama, M. Mukoujima, T. Kanda, S. Fujimoto, T. Kurosawa, H. Ishimabushi, K. Ishida, L. Rauscher, Y. Hata, Development of thermoelectric generating stacked modules aiming for 15% of conversion efficiency, in: *Thermoelectrics, 2005. ICT 2005. 24th International Conference on*, 2005, pp. 242–247.

[15] H.-S. Choi, W.-S. Seo, D.-K. Choi, Prediction of reliability on thermoelectric module through accelerated life test and Physics-of-failure, *Electron. Mater. Lett.* 7 (3) (2011) 271–275.

[16] X. Jiang, X. Zhang, J. Gao, Influence of structure parameters on performance of the thermoelectric module, *J. Wuhan Univ. Technology Mater. Sci. Ed.* 26 (3) (2011) 464–468.

[17] N.Q. Nguyen, K.V. Pochiraju, Behavior of thermoelectric generators exposed to transient heat sources, *Appl. Therm. Eng.* 51 (1) (2013) 1–9.

[18] T.H. Clin, S. Turenne, D. Vasilevskiy, R.A. Masut, Numerical simulation of the thermomechanical behavior of extruded bismuth telluride alloy module, *J. Electron. Mater.* 38 (7) (2009) 994–1001.

[19] A. Ziabari, E. Suhir, A. Shakouri, Minimizing thermally induced interfacial shearing stress in a thermoelectric module, in: *2012 18th International workshop on thermal investigations of ICS and systems (therminic)*, 2012.

[20] S. Turenne, T. Clin, D. Vasilevskiy, R.A. Masut, Finite element thermo-mechanical modeling of large area thermoelectric generators based on bismuth telluride alloys, *J. Electron. Mater.* 39 (9) (2010) 1926–1933.

[21] J.-L. Gao, Q.-G. Du, X.-D. Zhang, X.-Q. Jiang, Thermal stress analysis and structure parameter selection for a Bi2Te3-based thermoelectric module, *J. Electron. Mater.* 40 (5) (2011) 884–888.

[22] Y. Nakatani, T. Shindo, K. Wakamatsu, T. Hino, T. Ohishi, H. Matsumuro, Y. Itoh, Evaluation on thermo-mechanical integrity of thermoelectric module for heat recovery at low temperature, in: *Developments in Strategic Materials: Ceramic Engineering and Science Proceedings* vol. 29, 2008, pp. 69–76. Issue 10.

[23] A.S. Al-Merbat, B.S. Yilbas, A.Z. Sahin, Thermodynamics and thermal stress analysis of thermoelectric power generator: influence of pin geometry on device performance, *Appl. Therm. Eng.* 50 (1) (2013) 683–692.

[24] A.Z. Sahin, B.S. Yilbas, The thermoelement as thermoelectric power generator: effect of leg geometry on the efficiency and power generation, *Energy Convers. Manag.* 65 (2013) 26–32.

[25] Y. Li, X.Q. Yang, P.C. Zhai, Q.J. Zhang, Thermal stress simulation and optimum design of CoSb₃/Bi₂Te₃ thermoelectric unicouples with graded interlayers, in: *Multiscale and functionally graded materials 2006:(M&FGM 2006)*, vol. 973, 2008, pp. 297–302.

[26] M. Picard, S. Turenne, D. Vasilevskiy, R.A. Masut, Numerical simulation of performance and thermomechanical behavior of thermoelectric modules with segmented bismuth-telluride-based legs, *J. Electron. Mater.* 42 (7) (2013) 2343–2349.

[27] G. Chen, Y. Mu, P. Zhai, G. Li, Q. Zhang, An investigation on the coupled thermal–mechanical–electrical response of automobile thermoelectric materials and devices, *J. Electron. Mater.* 42 (7) (2013) 1762–1770.

[28] M. Zebarjadi, K. Esfarjani, M.S. Dresselhaus, Z.F. Ren, G. Chen, Perspectives on thermoelectrics: from fundamentals to device applications, *Energy Environ. Sci.* 5 (1) (2012) 5147–5162.

[29] L.E. Bell, Addressing the challenges of commercializing new thermoelectric materials, *J. Electron. Mater.* 38 (7) (2009) 1344–1349.

[30] R. McCarty, High performance from multiphysics coupled simulation, *ANSYS Adv.* II (2) (2008).

[31] ANSYS Inc., *Basic Analysis Guide Release 12.0*, 2009.

[32] Z. Wang, V. Leonov, P. Fiorini, C. Van Hoof, Realization of a wearable miniaturized thermoelectric generator for human body applications, *Sensors Actuators A Phys.* 156 (1) (2009) 95–102.

[33] B.C. Sales, D. Mandrus, B.C. Chakoumakos, V. Keppens, J.R. Thompson, Filled skutterudite antimonides: electron crystals and phonon glasses, *Phys. Rev. B* 56 (23) (1997) 15081.

[34] B. Duan, P. Zhai, L. Liu, Q. Zhang, Effects of double substitution with Ge and Te on thermoelectric properties of a skutterudite compound, *J. Electron. Mater.* 40 (5) (2011) 932–936.

[35] E. Sandoz-Rosado, R. Stevens, Robust finite element model for the design of thermoelectric modules, *J. Electron. Mater.* 39 (9) (2010) 1848–1855.

[36] Z.N. Cheng, G.Z. Wang, L. Chen, J. Wilde, K. Becker, Viscoplastic Anand model for solder alloys and its application, *Solder. Surf. Mt. Technol.* 12 (2) (2000) 31–36.

[37] J. Wilde, K. Becker, M. Thoben, W. Blum, T. Jupitz, G. Wang, Z.N. Cheng, Rate dependent constitutive relations based on Anand model for 92.5 Pb5Sn2. 5Ag solder, *Adv. Packag. IEEE Trans.* 23 (3) (2000) 408–414.

[38] T.-S. Oh, Thermoelectric characteristics of p-Type (Bi, Sb) 2Te3/(Pb, Sn) Te functional gradient materials with variation of the segment ratio, *J. Electron. Mater.* 38 (7) (2009) 1041–1047.

[39] L.N. Lukyanova, V.A. Kutasov, P.P. Konstantinov, V.V. Popov, Optimization of solid solutions based on bismuth and antimony chalcogenides above room temperature, in: *Modules, Systems, and Applications in Thermoelectrics*, vol. 2, CRC Press, 2012, pp. 1–18.

[40] R. Liu, P. Qiu, X. Chen, X. Huang, L. Chen, Composition optimization of p-type skutterudites CeyFexCo₄–xSb₁₂ and YbyFexCo₄–xSb₁₂, *J. Mater. Res.* 26 (15) (2011) 1813–1819.

[41] C.Y. Ho, M.W. Ackerman, K.Y. Wu, T.N. Havill, R.H. Bogaard, R.A. Matula, S.G. Oh, H.M. James, Electrical resistivity of ten selected binary alloy systems, *J. Phys. Chem. Ref. Data* 12 (2) (1983) 183–322.

[42] C.Y. Ho, M.W. Ackerman, K.Y. Wu, S.G. Oh, T.N. Havill, Thermal conductivity of ten selected binary alloy systems, *J. Phys. Chem. Ref. Data* 7 (3) (1978) 959–1178.

[43] P. Auerkari, *Mechanical and Physical Properties of Engineering Alumina Ceramics*, Technical Research Centre of Finland Finland, 1996.

[44] E. Çadırıllı, U. Büyük, H. Kaya, N. Maraslı, S. Aksöz, Y. Ocak, Dependence of electrical resistivity on temperature and Sn content in Pb-Sn solders, *J. Electron. Mater.* 40 (2) (2011) 195–200.

[45] B. Vandevelde, M. Gonzalez, P. Limaye, P. Ratchev, E. Beyne, Thermal cycling reliability of SnAgCu and SnPb solder joints: a comparison for several IC-packages, *Microelectron. Reliab.* 47 (2) (2007) 259–265.

[46] H.M. Ledbetter, E.R. Naimon, Elastic properties of metals and alloys. II. Copper, *J. Phys. Chem. Ref. Data* 3 (4) (1974) 897–935.

[47] Z. Guo, N. Saunders, P. Miodownik, J.-P. Schillé, Modeling material properties of lead-free solder alloys, *J. Electron. Mater.* 37 (1) (2008) 23–31.

[48] A. Zeanh, O. Dalverny, M. Karama, E. Woigard, S. Azzopardi, A. Bouzourene, J. Casutt, M. Mermet-Guyennet, Thermomechanical modelling and reliability study of an IGBT module for an aeronautical application, in: *Thermal, Mechanical and Multi-physics Simulation and Experiments in Microelectronics and Micro-systems, 2008. EuroSimE 2008. International Conference on*, 2008, pp. 1–7.

[49] C. Wu, Analysis of waste-heat thermoelectric power generators, *Appl. Therm. Eng.* 16 (1) (1996) 63–69.

[50] U. Erturun, K. Mossi, A feasibility investigation on improving structural integrity of thermoelectric modules with varying geometry, in: *ASME 2012 Conference on Smart Materials, Adaptive Structures and Intelligent Systems*, 2012, pp. 939–945.